

Continuum removal for ground based LWIR hyperspectral infrared imagery applying non-negative matrix factorization

BARDIA YOUSEFI^{1,*}, SAEED SOJASI¹, CLEMENTE IBARRA CASTANEDO¹, XAVIER P.V. MALDAGUE¹, GEORGES BEAUDOIN², AND MARTIN CHAMBERLAND³

¹Computer Vision and System Laboratory, Department of Electrical and Computer Engineering, Laval University, 1065, av. de la Médecine, Quebec, QC, Canada

²Department of Geology and Geological Engineering, Laval University, 1065, av. de la Médecine, Quebec, QC, Canada

³Telops, Inc., 100-2600 St-Jean-Baptiste Ave, Quebec City, QC, G2E 6J5, Canada

*Corresponding author: bardia.yousefi.1@ulaval.ca

Compiled July 24, 2018

Continuum removal is vital in hyperspectral image analysis. It enables data to be used for any application and usually requires approximations or assumptions to be made. One of these approximations is related to the calculation of the spectra of the background's blackbody temperature. Here, we present a new method to calculate the continuum removal process. The proposed method eliminates the calculation for ground-based hyperspectral infrared imagery by applying two acquisition sets before and after using the heating source. The approach involves a laboratory experiment on a long-wave infrared ($7.7\mu\text{m}$ to $11.8\mu\text{m}$ - LWIR), with a LWIR-macro lens, an Infragold plate and a heating source. To calculate the continuum removal process, the approach applies non-negative matrix factorization (NMF) to extract Rank-1 NMF, estimate the downwelling radiance and compare it with that of other conventional methods. NMF uses gradient-descent-based rules (GD) and non-negative least squares (NNLS) optimization algorithms to obtain Rank-1 NMF. A comparative analysis is performed with 1%~20% additive noise for all algorithms by using the spectral angle mapper and normalized cross correlation (NCC). Results reveal the promising performance of NMF-GD (average of 72.5% similarity percentage using NCC) and NMF-NNLS (average of 77.6% similarity percentage using NCC).

© 2018 Optical Society of America

OCIS codes: Long-wave infrared hyperspectral imaging; Continuum removal; spectral comparison method; Ground based hyperspectral imagery; Mineral identification.

<https://doi.org/10.1364/AO.57.006219>

This manuscript is an author version and the main article can be found in Applied Optics journal [1].

1. INTRODUCTION

Hyperspectral infrared imagery has been used in remote sensing and airborne imaging in the past three decades. Apart from optical and thermographic equipment improvements, the process and data mining developments in this field have also displayed remarkable growth and have been adopted in various applications, such as target detection [2, 3], aviation [4], spectral unmixing [5] and geology [6–9]. An important element in successful data analysis is proper spectral information retrieval, that is, continuum removal (CR), at the beginning of the analysis. A continuum in hyperspectral infrared imagery is mainly caused by solar energy or the heating source. Many methods have been developed to retrieve spectra and perform CR. These methods were proposed for remote sensing, airborne-type data analysis [10, 11], endmember-based algorithms [12] and retrieval of emissivity and downwelling radiation by using the spectral radiance of rocks [13]. The process for ground-based hyperspectral imagery [6, 7, 14, 15] is similar but involves close-range acquisitions. It has

been extensively used in different applications, including quality control in chemical reactions [16, 17], raw material sorting in the tobacco industry [18], investigation of anomalies in target detection [19], checking of exhaust from diesel-fuelled turbine technologies [20] and geology [13]. Active-thermography ground-based close-range imagery allows for the use of a heating source in the place of any other source (e.g. solar energy in airborne or remote sensing applications). The process of hyperspectral analysis is similar in long- and close-range hyperspectral imagery, but the use of a heating source usually allows for increased control on the experiment [21]. One of the early studies on determining sample emissivity was conducted by Salisbury et al. (1991) [22], who estimated the reflectance and transmittance spectra of 78 minerals in mid-wavelength infrared. The authors calculated the effect of different particle size ranges and the scattering effect. Thermal infrared for remote sensing and Kirchhoff's law were investigated for directional hemispherical reflectance and directional emittance measurements of rock and soil in a laboratory [23]. Korb et al. (1996) calculated the radiance (downwelling) and emissivity for a Fourier transform infrared spectroradiometer (FTIR) for 3–5 μm and 8–14 μm atmospheric windows [24], followed by the development of the μFTIR system [25] and laboratory technique for measurement and calibration [26] and for the emissivity and reflectance of soil [27]. Gomez et al. (2008) also presented a partial least-squares regression (PLSR) method for clay and calcium carbonate content estimation at visible and near-infrared (VNIR, 400–1200 nm) and shortwave infrared (SWIR, 1200–2500 nm) for airborne hyperspectral measurements [28]. Malenovsky et al. (2013) proposed a neural network-based CR for spruce leaf chlorophyll content estimation [29]. The continuum-removed absorption features used for predicting in situ pasture quality adopted the standard first derivative reflectance (FDR), band depth (BD) and band depth ratio (BDR) in airborne imaging spectrometers [30]. Moreover, a continuum removal analysis was performed in a previous study to estimate foliage nitrogen concentration in HYMAP sensor data by using modified partial-least squares (MPLS) [31]. Balick et al. (2009) [13] presented an emissivity retrieval method using field-portable imaging radiometric spectrometer technology mid-wave extended (FIRST-MWE) and calculated atmospheric downwelling spectral radiance. The research involved a

similar continuum removal method although the calculation was for non-ground based spectroscopy. The proposed approach modifies the Balick method [13] by eliminating its dependency on the blackbody spectra at surface temperature. Our approach involves a series of experiments conducted using a Telops Long Wave Infrared (LWIR) hyperspectral camera in close range for small mineral grains. Moreover, the approach proposes another modification for CR calculation by applying first-rank NMF instead of the previously used spectral averaging or random selection of spectra, thus increasing efficiency. The remainder of the paper is organized as follows. Section 2 provides information about the hyperspectral infrared camera and targeted minerals. Section 3 presents the methodology and explains how continuum removal and segmentation are performed. Section 4 describes the experimental and simulation results. A short discussion is presented in Section 5, and the conclusions and directions for future work are provided in Section 6.

2. DATA

A. Sensor

The sensor used to make the measurements was a lightweight FIRST hyper-camera imaging spectroradiometer (HYPER-CAM LW) [32] operating in the long-wave infrared (LWIR) band (from 7.7 to 11.8 μm). The sensor has a Stirling-cooled indium antimonide (InSb) focal plane array (FPA) that contains 320×256 pixels. It has a spectral resolution of 0.25 cm^{-1} . The spectral resolution of the spectrometer,

Table 1. A brief review of the characteristics of the minerals investigated in this study.

Minerals	Chemical formula	Short Description
Biotite	$\text{K}(\text{Mg,Fe})_{2-3}\text{Al}_{1-2}\text{Si}_{2-3}\text{O}_{10}(\text{OH,F})_2$	substantial group of dark mica minerals.
Diopside	$\text{MgCaSi}_2\text{O}_6$	Forms complete solid solution series with hedenbergite ($\text{FeCaSi}_2\text{O}_6$) and augite, and partial solid solutions with orthopyroxene and pigeonite. silicate mineral.
Epidote	$\text{Ca}_2(\text{Al}_2\text{Fe})(\text{SiO}_4)(\text{Si}_2\text{O}_7)\text{O}(\text{OH})$	silicate mineral.
Tourmaline	$(\text{Na, Ca})(\text{Mg,Li,Al,Fe}^{2+})_3\text{Al}_6(\text{BO}_3)_3\text{Si}_6\text{O}_{18}(\text{O,H})_4$	boron silicate minerals compounded with element such as Al, Fe, Mg, Na, Li or K.
Olivine	$(\text{Mg}^{+2}, \text{Fe}^{+2})_2\text{SiO}_4$	
Pyrope	$\text{Mg}_3\text{Al}_2(\text{SiO}_4)_3$	garnet group minerals.
Quartz	SiO_2	the most abundant mineral in the Earth's crust.

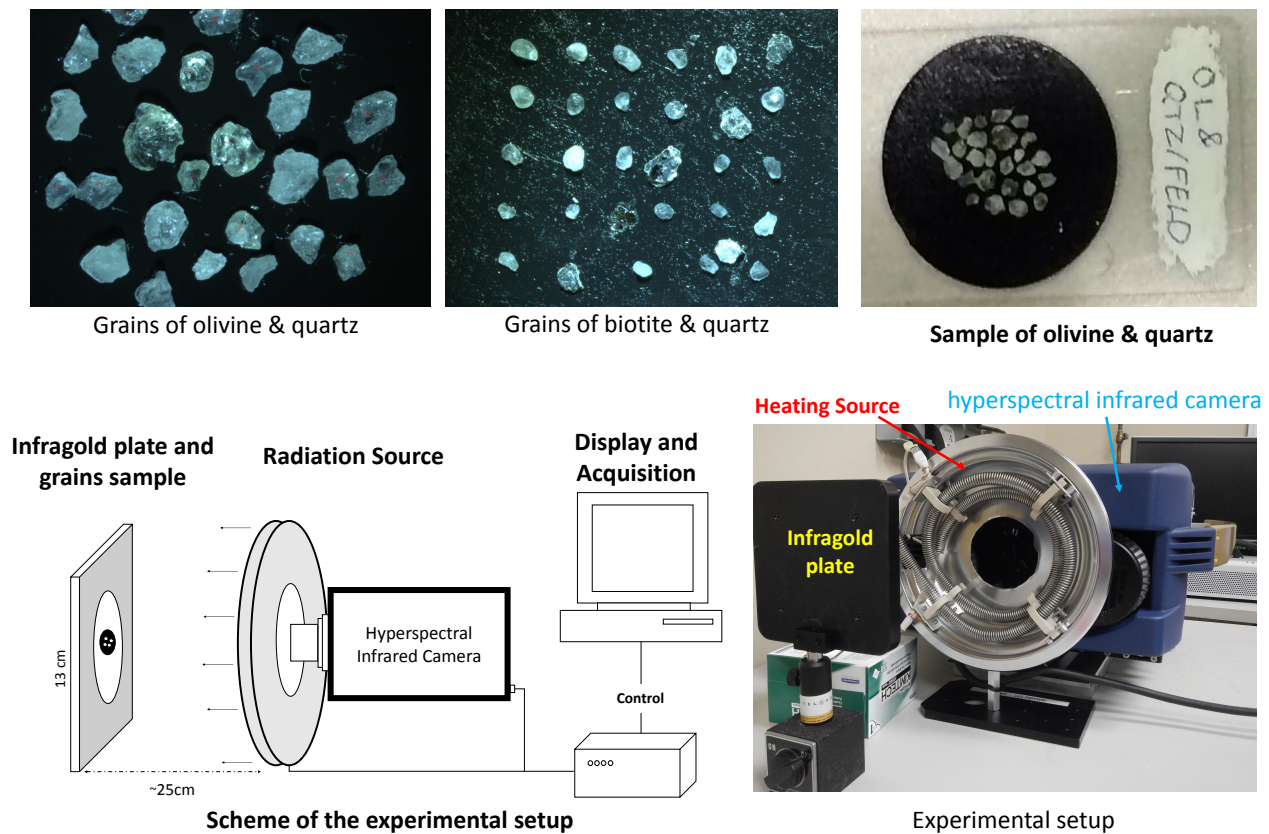


Fig. 1. The experimental setup is shown along with the binocular image of the samples and the scheme of the experimental setup.

6 cm^{-1} ($\sim 0.0119\mu\text{m}$ at $7.7\mu\text{m}$ and $\sim 0 : 0465\mu\text{m}$ at $11.8\mu\text{m}$), provided 88 spectral bands. The spatial extent of the scene was windowed to a small field of view (FOV) to increase the temporal resolution. The spectra were measured using a Fourier transform spectrometer (FTS), and the hyper-camera measured a complete spectrum for every pixel using an LW macro $50 \times 10^4\mu\text{m}$ lens providing an instantaneous FOV of 0.35 mrad [32]. Measurements were performed from a distance of 35 cm , which provided a pixel footprint of $0.1 \times 10^4\mu\text{m}$. Figure 1 presents the experimental setup and binocular images of the samples. A heating source was placed in front of the samples (active thermography¹) and provided heating energy during the experiment. Image acquisition was continued after turning off the heating source to achieve a gradual cooling effect

¹Active thermography occurs once an energy source creates thermal contrast for the specimens and background [33]. An example of active thermography was provided in [34].

(several minutes). For optimal results, the grains were attached to adhesive carbon-based tape, and an Infragold plate was placed on the background. Its reflectance assisted in removing the continuum from the spectrum. The images were obtained perpendicular to the mineral grains under uniform heating by the source.

B. Grain samples and reference panels

The problem of spatial resolution was not an issue because a magnification lens was used for the FOV of the sensor. Figure 1 shows a photograph of the minerals obtained with a binocular microscope and the scheme of the experimental setup. Seven mineral grains (biotite, diopside, epidote, tourmaline, pyrope, olivine and quartz) are presented in Table 1, which provides a brief review of the minerals and their chemical formulas. A square InfraGold® plate (Labsphere, North Sutton, NH, USA) [35] was placed

in the scene of the grains as a reference panel. According to the information provided by the manufacturer, the panel has a reflectivity of 92%–96% for $10^4\mu\text{m}$ to $16 \times 10^4\mu\text{m}$ wavelength radiation. For the range of the FIRST camera, the spectral reflectance is approximately between 96% and 97% by Duraflect® coatings of 0.94–0.96 [35]. The emissivity of the panel is very low, which makes it insensitive to temperature. The panel was placed in a perpendicular position in front of the hyperspectral camera.

3. ANALYSIS

Here, the proposed method is presented by downwelling radiance calculation, continuum removal and Infragold and thermal image analyses using Rank¹ NMF (Figure 2 presents the flowchart of proposed approach).

A. Downwelling radiance calculation

Following the protocols for accurate determination of sample emissivity [24–26, 36] and considering the modification of Balick et al. (2009) [13] while noting that the distance between the samples and camera is short, the downwelling spectral radiance ($L_i(\lambda)$) in the atmospheric environment was calculated with the equation

$$L_i(\lambda) = \frac{L^*(\lambda) - \varepsilon BB(\lambda, T_s)}{\rho} \quad (1)$$

where L^* is the measured spectral radiance of the panel and $BB(\lambda, T_s)$ is the spectra of the blackbody at a surface temperature of T_s . ε and ρ are the emissivity and reflectivity of the panel, respectively [13]. In ideal conditions, the surface temperature of the panel and the measured temperature are similar. Considering that the specimen has a very low transmission of infrared energy (~ 0), then according to Kirchhoff's law [23, 37], $1 = \varepsilon + \rho$. Thus, the aforementioned equation can be rewritten based on the measured spectral radiance.

$$L^*(\lambda) = \varepsilon BB(\lambda, T_s) + (1 - \varepsilon)L_i(\lambda) \quad (2)$$

The measured spectral radiance is a parameter that is related to the emissivity of the panel and blackbody spectral radiance.

B. Continuum removal

To calculate the reflectance spectrum that contains no continuum, the measured spectral radiance of the

specimen was divided by the entire spectrum radiated from the heating source (Fig. 3). The Infragold® plate was used to estimate the total radiance from the source (or downwelling radiance L_i) because it ideally reflects $\sim 100\%$ of the input radiance. Given that these experiments strive to calculate the ground spectra and control of the heat source is possible, we performed image acquisition twice: once while the heating source was switched on and once while the heating source was switched off (7). Then, we obtained

$$\begin{cases} L_{ON}^*(\lambda) = \varepsilon BB(\lambda, T_s) + (1 - \varepsilon)L_{iON}(\lambda) \\ L_{OFF}^*(\lambda) = \varepsilon BB(\lambda, T_s) + (1 - \varepsilon)L_{iOFF}(\lambda) \end{cases} \quad (3)$$

Considering that the temperature of the blackbody with or without heating is the same, if we subtract the two previous equations from each other. Then the blackbody spectral radiance of the panel at the surface temperature, $BB(\lambda, T_s)$, and the emissivity of the plate, ε , have the same value when the heating source is in the circuit or out of the experiment. Thus, the return radiance amount from the mineral grain is given by

$$L_{ON}^*(\lambda) - L_{OFF}^*(\lambda) = (1 - \varepsilon)(L_{iON}(\lambda) - L_{iOFF}(\lambda)) \quad (4)$$

The reflectivity spectra of a factor that is independent of the blackbody spectral radiance were then calculated, and we obtained

$$\rho = \frac{L_{ON}^*(\lambda) - L_{OFF}^*(\lambda)}{L_{iON}(\lambda) - L_{iOFF}(\lambda)} \quad (5)$$

This equation has reflectivity spectral radiance whose continuum is already suppressed. Equation (6) represents the continuum removal for our ground-based spectra that is solely dependent on the measured spectral radiance from the surface of mineral grains and the Infragold® plate. In the equation, $L_{iON}(\lambda)$ and $(L_{iOFF}(\lambda))$ are having the pixel-scale dependency of the downwelling spectral radiance.

C. Infragold and thermal image analysis using Rank-1 NMF

Following Equation (6), the spectral radiance of the Infragold® plate is needed to calculate the downwelling spectral radiance L_i (for L_{iON} and L_{iOFF}). Since the Infragold® plate reflects the entire radiance, we calculated a representative spectral

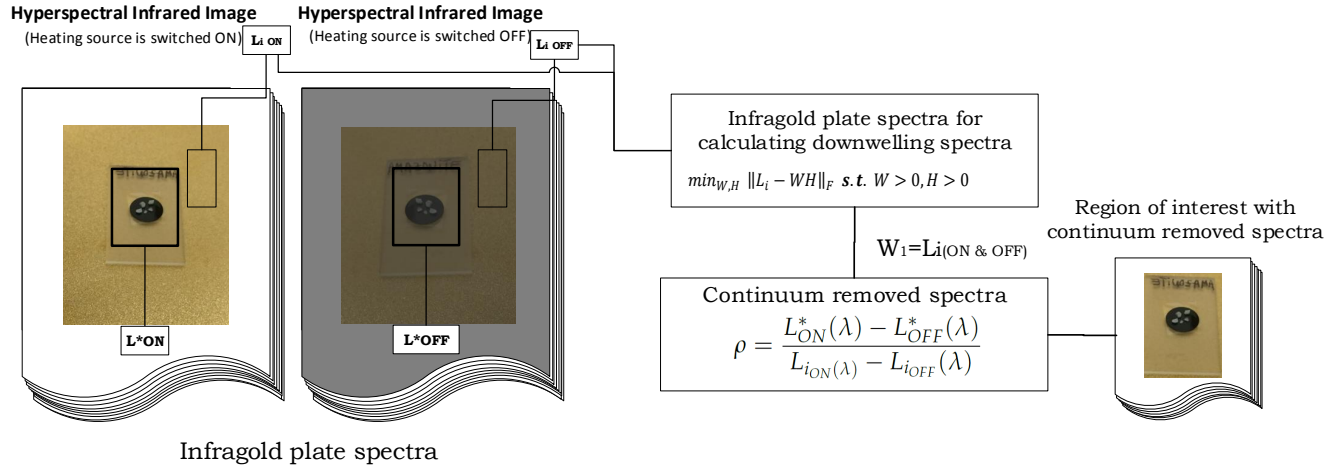


Fig. 2. Flowchart which shows the proposed approach for the estimation of the downwelling radiance among all the possible points. In the figure, $W_1 = L_{i(ON\&OFF)}$ represents the spectral of Infragold with and without the heating source.

radiance to include in Equation (6). To measure the spectral radiance, some pixel spectra in Infragold were manually selected and used to calculate downwelling radiance. Multifarious techniques, such as random selection and spectra averaging, are often adopted to achieve this purpose, but these techniques are attenuated when faced with noise or incorrect selection of the Infragold region. Random selection of downwelling spectral radiance is not an appropriate means of determining the spectra because this method may select the wrong spectrum. By contrast, spectral averaging is a more reasonable means to estimate the spectra, but it is theoretically insensitive to non-homogeneous spectral grouping. For example, if the selected region of the Infragold® plate extends beyond the plate itself, the averaging might be influenced by the spectral radiance of other regions. Several other approaches, such as eigen decomposition methods, improve spectrum selection [38, 39]. For example, principal component analysis (PCA) [40, 41] is a popular method that can select the principal component spectrum of a selected region, but having negative values in its calculation leads to an uncertainty in its application in choosing the best representation of reconstructed spectra (first basis vector). This problem is solved by different modifications (such as [42]) or non-negative matrix factorization (NMF) [43–45].

The approach presented in this study calculates

the aforementioned radiance (particularly for a non-uniform heating source) by applying NMF. NMF is a factor analysis method that provides an unsupervised linear representation of the data similar to PCA. However, by using non-negative coefficients in the calculation of eigenvalues, the issue with PCA is solved. NMF produces the basis from data representations and can be formulated using the following optimization problem [46].

$$\min_{W,H} \|L_i - WH\|_F \quad s.t. \quad W \geq 0, H \geq 0 \quad (6)$$

L_i refers to all possible points of spectral radiance in the Infragold plate while the heating source is switched on and off, with the assumption that the measured T in our data consists of N non-negative scalar variables.

$$L_{N \times M} \approx W_{N \times T} H_{T \times M} \quad (7)$$

W is an $N \times T$ matrix that includes the basis vectors \vec{w}_i as its columns. Every measured vector is shown by the same basis vectors. W has T basis vectors and can be represented by "building blocks" of the data having T -dimension. H denotes the coefficient matrix and explains the level of power for every building block, where \vec{l} is a measurement vector. H includes the coefficient vector corresponding to the measurement vector \vec{l} , which produces a linear data representation obtained from data factorization. W contains the basis vectors that are needed to deter-

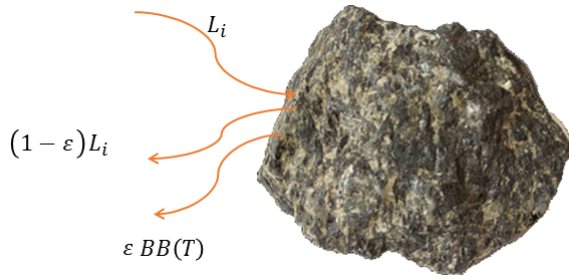


Fig. 3. The spectral radiance from the source and its reflection from the mineral grain is shown.

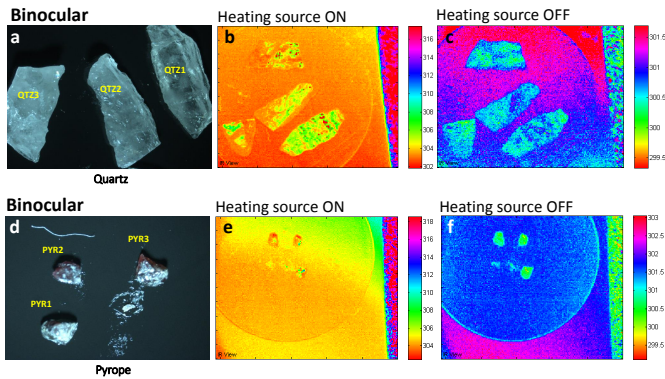


Fig. 4. The IR-images were taken before (left-side thermal images in each mineral(c,f)) and after (right-side thermal images in each mineral (b,e)) heating the mineral grains. The binocular images from the grains are also shown on left side of each example (a,d).

mine the best representative of spectral radiance and is even used for clustering [45, 47].

$$L_{N \times M} = \begin{bmatrix} \vec{l}_1 \\ \vec{l}_2 \\ \cdot \\ \cdot \\ \vec{l}_t \end{bmatrix} W_{N \times T} = \begin{bmatrix} \vec{w}_1 \\ \vec{w}_2 \\ \cdot \\ \cdot \\ \vec{w}_n \end{bmatrix} \quad (8)$$

In the equation, \vec{l}_1 shows the first pixel spectrum selected from the Infragold plate that has \vec{w}_1 basis vectors corresponding to it. This case is used for the extraction of the best spectral representative of the Infragold plate (downwelling spectrum), \vec{w}_1 . NMF performs as a clustering method to group the spectra in different categories (similar to [45]), whereas Rank-1 NMF does not allow further grouping be-

cause it limits the clustering to abundant spectra existing in the input data (ROI mainly consists of the Infragold region). NMF through GD converts the minimization problem to a first-order iterative optimization algorithm which is one of the simplest methods but claims to be a slow algorithm. It finds the local minimum by applying gradient calculation and its direction towards the minimization through steps proportional to the negative gradient from the current point. If Equation (7) is represented by $G(w)$ and w_t represents the current observation point, then the minimization w_{t+1} should be selected based on $w_{t+1} = w_t - \gamma G(w_t)$, where γ is the step size and $G(w_t) \geq G(w_{t+1})$ [48]. This way is chosen because the speed of algorithm was not an issue for this application and there is mineral concentration in the experimental results where the components of data have necessarily nonnegative. NMF is still considered a linear method for non-negative approximation (standard NMF can be calculated by two optimization algorithms: gradient-descent (GD) and non-negative least squares (NNLS)) [42, 45, 49]. NNLS is a constrained form of the least-squares problem and applies a similar minimization strategy for the minimization of NMF, considering the non-negative constraints to control the coefficients. NMF is applied by NNLS to Equation (7), given a matrix W and vectorized matrix L_i . The goal is to solve the Euclidean norm problem and ultimately perform the mentioned minimization by the respect to the Karush-Kuhn-Tucker (KKT) conditions [50, 51] by the general form of multiple right-hand sides for $\min_{W^T > 0} |H^T W^T - L_i|_F^2$, which can be decoupled into the coefficient's dimension with the single right-hand side [51] (the general W update follows GD having NNLS constraints).

D. Spectral comparison methods

Spectral angle mapper (SAM) is a method based on the physical property of a spectrum. It provides features for discrimination among spectra through an error generated by the angle difference between two vectors (target spectrum and its reference). SAM is used for n-dimensional geometrical space and determines the dissimilarity between the unknown spectrum w and the reference spectrum r by using the equation [52]

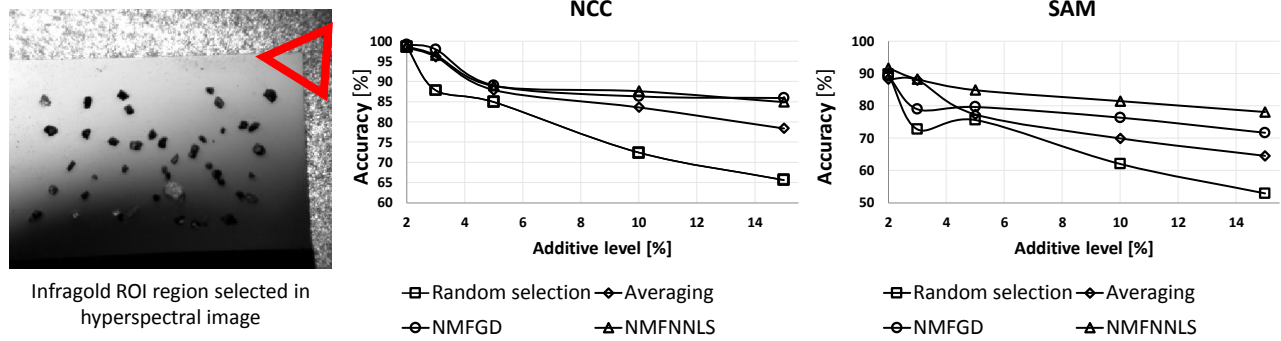


Fig. 5. The similarity percentage of spectra while Infragold region wrongly selected based on the mis-selection percentage is also mentioned.

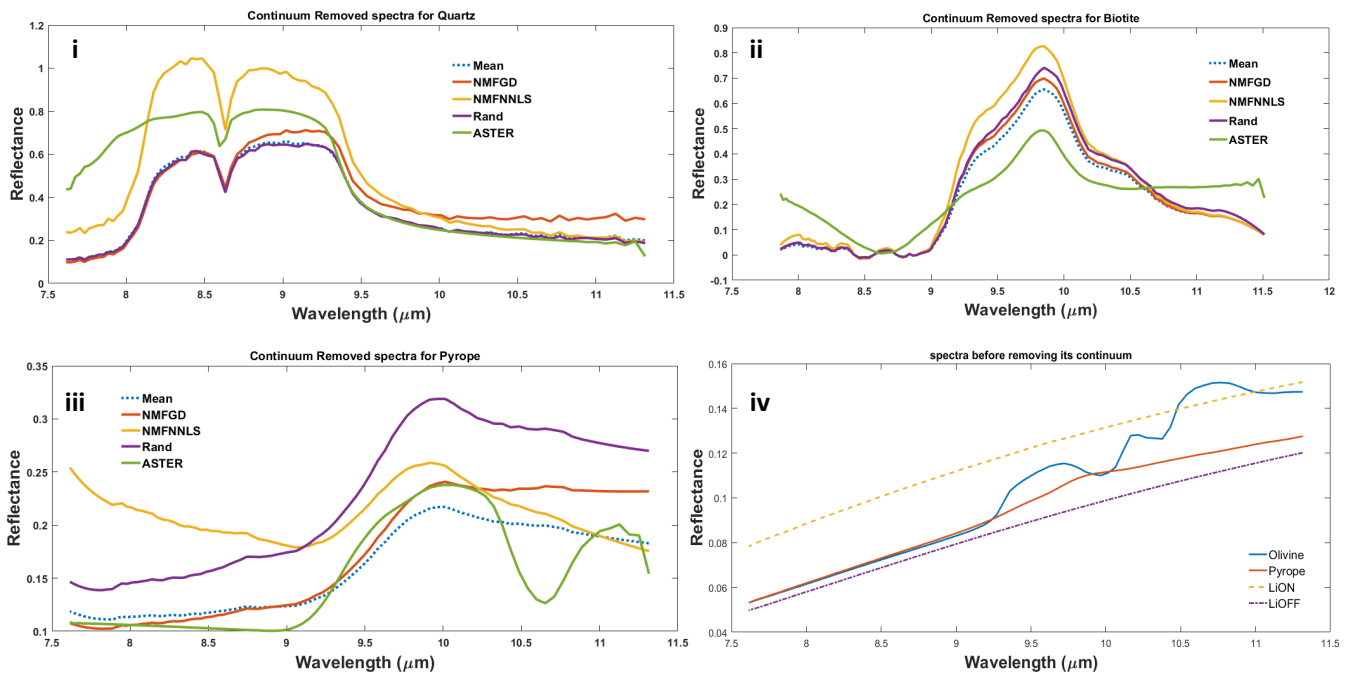


Fig. 6. Some examples of the continuum removed spectra of pyrope, and quartz in the $7.7 \mu\text{m}$ to $11.8 \mu\text{m}$ wavelength range are shown. The plot diagrams in each mineral depicts the spectra for the Infragold plate and some spectra from the surface of the mineral while the heating source is On and Off. Spectral radiance corresponding to the Infragold plate and three minerals space (quartz, biotite, and pyrope) are also shown in **i,ii,iii**. The spectral of radiance the Infragold panel and spectral of Olivine before continuum removal process are shown (**iv**). The downwelling radiance is calculated by subtracting these two spectra. The downwelling spectra of the other minerals are shown using this subtraction and presented with the reference spectra of the targeted mineral from the ASTER library.

$$\alpha = \cos^{-1} \left[\frac{\sum_{i=1}^N w_i r_i}{\left[\sum_{i=1}^N w_i^2 \right]^{1/2} \left[\sum_{i=1}^N r_i^2 \right]^{1/2}} \right] \quad (9)$$

where N is the number of bands. For each pixel spectrum selected in the hyperspectral image cube, the spectral angle reference spectrum calculates an error. The radian values regarding every corresponding

Table 2. The similarity percentage of the continuum removed approach in comparison with the reference spectra from the ASTER/JPL spectral library is measured. Also the robustness of the approach is shown applying additive noise.

Mineral	Noise	Method (%)							
		NCC				SAM			
		Average	NMFGD	NMFNNLS	Random selection	Average	NMFGD	NMFNNLS	Random selection
Biotite	0%	90.3	89.9	86.8	90.1	72.3	71.9	69.9	72.2
	1%	93.1	92.9	89.9	90.2	78.9	78.8	76.5	73.5
	2%	89.3	89.3	85.2	75.1	70.9	70.9	68.3	51.2
	5%	92.9	91.7	89.4	21.4	78.7	76.9	75.9	<1
	10%	89.2	78.5	83.2	6.3	70.9	59.2	64.7	<1
Diopside	0%	74.1	66.4	76.3	<1	62.2	49.8	59.8	<1
	1%	72.2	72.8	74.3	71.8	57.5	58.3	60.8	56.9
	2%	71.4	71.2	74.2	69.7	57.9	57.6	62.6	57.1
	5%	71.8	72.5	75.4	64.5	57.8	58.6	62.7	49.4
	10%	71.7	70.4	73.6	16.8	57.7	57.1	60.8	<1
Epidote	0%	71.5	56.2	71.5	<1	57.7	40.9	59.01	<1
	1%	68.4	51.1	69.2	<1	56.8	38.5	57.4	<1
	2%	84.4	82.1	84.8	84.6	66.1	62.8	68.4	66.4
	5%	85.3	85.7	87.7	82.8	63.5	63.9	67.2	61.6
	10%	82.8	82.9	86.8	79.9	64.1	64.3	69.8	61.7
Tourmaline	0%	84.3	84.7	83.9	4.8	65.9	65.5	67.2	<1
	1%	79.8	57.9	81.1	<1	62.7	39.7	63.9	<1
	2%	76.2	44.1	77.02	<1	61.4	28.02	61.8	<1
	5%	52.6	51.9	53.4	52.1	38.5	33.2	32.9	32.9
	1%	47.5	47.8	50.4	46.5	36.9	37.2	40.1	35.4
Pyrope	0%	47.4	48.1	51.1	43.2	36.9	37.4	39.7	35.2
	1%	46.5	45.9	47.1	7.6	35.1	34.6	35.2	<1
	2%	46.5	29.6	55.9	9.6	30.3	26.8	34.1	<1
	5%	50.8	29.6	55.9	9.6	30.3	26.8	34.1	<1
	10%	45.7	12.1	52.8	<1	28.01	22.9	31.2	<1
Olivine	0%	93.5	94.1	75.4	93.5	44.9	46.1	28.4	44.5
	1%	93.9	93.9	86.6	88.4	54.8	56.1	41.5	51.8
	2%	92.7	93.4	85.9	75.2	55.8	56.5	43.1	48.3
	5%	92.2	93.3	87.5	4.1	62.3	63.7	53.1	<1
	10%	92.9	55.9	84.2	<1	56.2	33.3	45.1	<1
Quartz	0%	87.01	32.2	81.2	<1	52.2	28.2	42.1	<1
	1%	84.9	84.9	80.8	84.7	64.9	64.6	56.8	64.5
	2%	86.4	86.1	85.5	86.1	66.7	66.01	64.2	66.4
	5%	87.6	88.2	87.2	75.5	68.3	69.1	65.7	53.9
	10%	86.1	82.1	81.1	16.01	65.9	61.7	58.3	<1
Quartz	0%	86.1	28.1	81.1	<1	65.8	51.4	59.2	<1
	1%	80.9	21.5	80.4	<1	61.2	47.5	57.9	<1
	2%	73.6	75.2	82.3	75.3	62.2	62.8	65	62.5
	5%	70.4	69.6	80.7	66.5	61.9	61.7	65.9	58.7
	10%	73.5	75.5	80.3	64.1	62.1	62.9	63.3	53.7
Quartz	0%	68.6	63.4	77.1	11.6	63.7	57.5	66.8	<1
	1%	69.7	50.5	73.3	11.8	61.5	38.8	60.3	<1
	2%	64.2	47.9	70.6	5.8	57.3	28.1	57.8	<1
	5%	64.2	47.9	70.6	5.8	57.3	28.1	57.8	<1
	10%	64.2	47.9	70.6	5.8	57.3	28.1	57.8	<1

pixel at the output of SAM represent the difference in the spectral vector direction from that of the reference.

Normalized cross correlation (NCC) is a method to determine the correlation between two spectral data. NCC uses two types of entry: the data and their reference. It uses a formula for r through substitution-estimation of the covariances and variances

based on a sample in the formula. If the dataset presented by \vec{w}_t includes N values and $\{r_1, \dots, r_N\}$ presents another dataset having N values, then the formula for r is

$$NCC = \frac{1}{N} \sum \frac{1}{\sigma_{w_t} \sigma_{r_{Ref}}} (w_t r_{Ref}). \quad (10)$$

where N is the number of pixel spectrum in w_t and r_{Ref} (w_t and r_{Ref} are normalized) and σ_{w_t} and r_{Ref} are standard deviations of w_t (data vector) and r (reference spectra) sets, respectively.

4. RESULTS

A selected set of the spectra from the targeted minerals is given in Figure 6 along with the calculation of downwelling spectral radiance for the selected minerals. The proposed approach presented two novelties, namely, spectral (radiometric) information and statistical analysis. The computational analysis of hyperspectral data from both perspectives are presented here. The continuum-removed spectra using random selection, averaging, NMF-GD and NMF-NNLS for downwelling radiance are shown in Figures 6 i-iv. To compare the different radiance calculated by different methods, all radiance spectra are presented on the same graphs. For a more quantitative assessment of the spectra obtained by each method, a reference spectral library was used, and the difference between targeted and reference spectra was calculated. The Advanced Space-borne Thermal Emission and Reflection Radiometer (ASTER) [53] library contains the spectra of nearly 2000 types of soils, rocks, minerals, snow, water and artificial minerals. Several of these spectra cover the wavelengths measured in this study (0.4–14 μm). The spectral data for each mineral cover visible, near-IR, mid-IR and thermal-IR wavelengths.

The difference between targeted and reference spectra was obtained using NCC and SAM. The main difficulties were related to using two different spectral resolutions in the calculation, which was performed by downsampling the high spectral resolution to a low resolution. Thus, NCC and SAM were applied to the four continuum-removed spectra obtained (spectral averaging, NMF-GD, NMF-NNLS and random selection). The computation results are presented in Figure 5 and Table 2 in percentages that express the quantitative similarity of these spectra with the reference spectra for additive noise (high frequency controlled magnitude random signal) and mis-selection of the Infragold plate, respectively. The level of similarity was reduced by adding noise for all of the methods, but random selection of spectra showed the highest sensitivity against noise compared with the three other methods. At a high level of noise, NMF showed a robust behavior (with the exception of pyrope and olivine). At a low level

of additive noise, NMF-NNLS showed considerably higher robustness in the presence of noise for diopside, epidote, tourmaline and quartz, whereas in the pyrope case, NMF-GD showed higher robustness compared with the other methods. This result is due to the minimal dependency of NNLS on the amplitude of spectra in the calculation compared with the other methods involving NMF-GD, averaging and random selection of spectra (Figure 6). The signal-to-noise Ratio (SNR) was calculated for this approach by following the formulation

$$SNR = \frac{\mu_S}{\sigma_N} \quad (11)$$

where μ_S and σ_N are the average of the signal (spectra) in the ROI region in the hyperspectral image and the standard deviation of noise, respectively (Figure 7 shows the graph of SNR when the additive noise level increases). Spectral averaging showed higher similarity with the reference spectra for biotite and olivine because of the higher reflectance of these minerals compared with the other minerals (Table 2). In general, SAM produced a lower similarity percentage compared with NCC, but the similarity trend was nearly the same. Figure 5 shows the similarity percentage when the Infragold ROI includes other parts of the hyperspectral image (this region was added by additive pixel-spectral percentage). The results presented in Figure 5 reveal the higher robustness of averaging compared with random selection and the higher similarity measure for NMF compared with the two other methods (with the exception of 3% where the similarity of averaging is higher than that of NMF-GD).

The computation complexity (in seconds) of these

Table 3. Comparative accuracy of the proposed approach is shown with PLSR.

Average NCC	Comparative accuracy				
	PLSR	Random selection	Averaging	NMFGD	NMFNNLS
Biotite	63.2	90.1	90.3	89.9	86.8
Diopside	61.2	71.8	72.2	72.8	74.3
Epidote	68.8	84.6	84.4	82.1	84.8
Tourmaline	44.7	52.6	51.9	53.4	52.1
Pyrope	90.1	93.5	93.5	94.1	75.4
Olivine	69.6	84.7	84.9	84.9	80.8
Quartz	70.7	75.3	73.6	75.2	82.3

calculations is presented in Table 4. NMF-GD and NMF-NNLS calculations proceeded for 1000 and 200 iterations, respectively. The computation of these algorithms was about 20 times more demanding than that of the algorithms for random and average selection of radiance. NMF-NNLS showed a higher computational complexity than NMF-GD, thus indicating the difference between a first-order iterative optimization algorithm and a constrained version of the least-squares problem, which is equivalent to a quadratic programming problem [54]. The average accuracy of the proposed approach was compared with that of previous methods (PLSR) [28, 31], as shown in Table 3. For each method, continuum removal was calculated and compared using NCC to its corresponding spectra in ASTER/JPL. To calculate the continuum removal using PLSR, the spectral radiance with heating source was used to estimate the continuum. The results of the comparison indicated that the proposed approach (using spectral radiance without a heating source) has a high average accuracy in suppressing the spectral continuum from spectra (ACC) is: $ACC_{NMF-GD} = 78.9\%$, $ACC_{NMF-NNLS} = 76.7\%$, $ACC_{Averaging} = 78.6\%$, $ACC_{Random} = 78.8\%$, $ACC_{PLSR} = 66.9\%$ [55].

5. DISCUSSION

The presented approach proposes a new modification of the continuum removal technique for ground-based hyperspectral imagery. The method facilitates the calculation of continuum removal for hyperspectral image acquisitions with and without a heating source. This feature alleviates the difficulty of the

Table 4. The computational time (CPU time) is shown for each part of the method for around 1000 pixels of Infragold plate.

Mineral	Computational Complexity			
	Averaging	NMF-GD	NMF-NNLS	Random
Biotite	0.2	0.79	1.18	0.28
Diopside	0.18	0.68	1.31	0.28
Epidote	0.18	0.98	1.33	0.26
Tourmaline	0.18	0.62	1.32	0.26
Pyrope	0.16	0.60	1.21	0.23
Olivine	0.17	0.76	1.11	0.23
Quartz	0.19	0.79	1.12	0.24

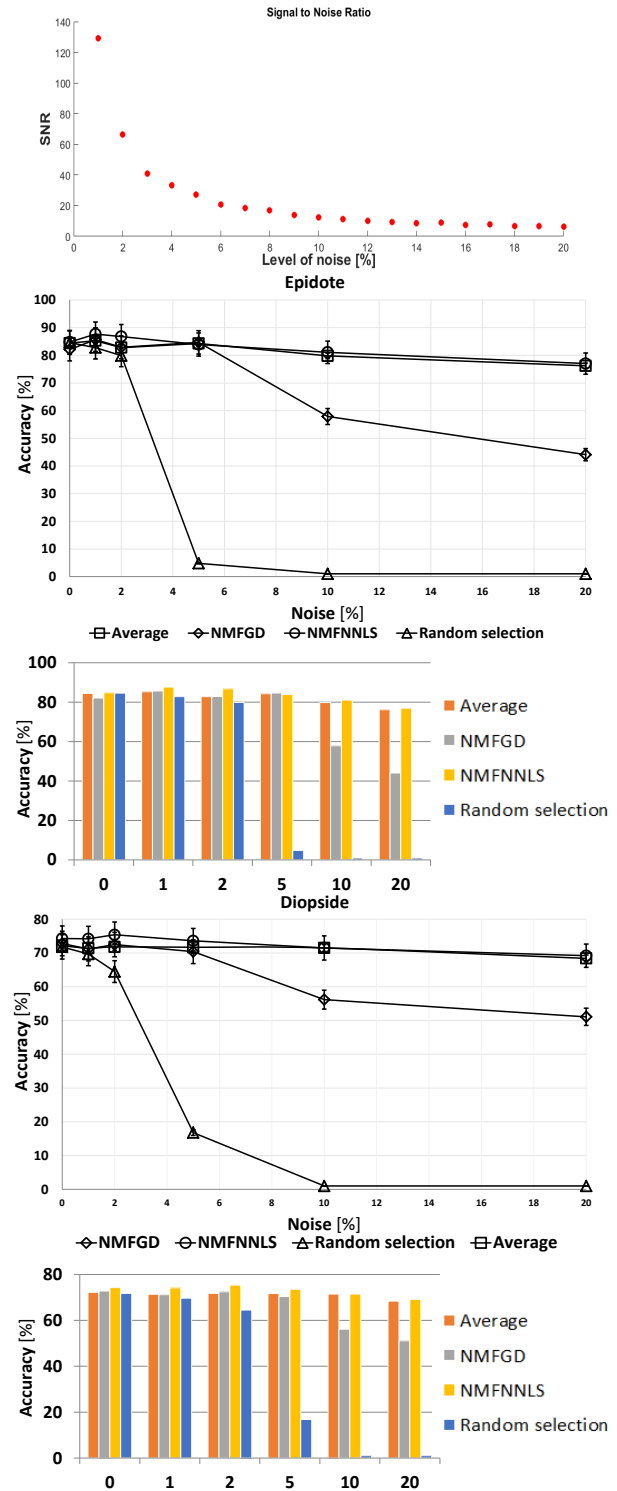


Fig. 7. Signal to noise ratio along with similarity level of continuum removed to ASTER/JPL spectral library are shown.

process by suppressing the blackbody temperature on the panel's surface. An experiment was conducted within the $7.7\mu\text{m}$ to $11.8\mu\text{m}$ LWIR wavelength

range using a FIRST FTIR LW hyperspectral camera of Telops. Another novelty of this approach is related to applying NMF analysis to downwelling radiance. The proposed algorithm uses Rank-1 NMF to determine the downwelling radiance and ensures the best basis radiance selection. The application of NMF in comparison with other linear Eigen decomposition methods (e.g. PCA [41]) showed better basis representative calculation due to non-negative coefficients in the process [44]. Negative coefficients indicate the relationships among some of the bases that occurs in eigen decomposition approaches, such as PCA. In addition, Rank-1 NMF represents the basis corresponding to the heat matrix in the factorization process, which is a guarantee for obtaining a better representative of the input data (downwelling radiance set) [45]. The standard NMF optimized by GD and NNLS algorithms were tested for the evaluation of the performance of Rank-1 NMF calculation from downwelling radiance through each of these algorithms. These results were in agreement with those obtained using the averaging and random selection of spectra. The use of random spectrum selection from the Infragold® panels provided a sensitive radiance that did not reliably denote the downwelling radiance. Furthermore, incorrect selection of the Infragold® panel (in the image) for spectrum calculation is another potential source of error that may influence the calculation. The application of NMF provided a solution and led to enhanced robustness in the presence of such complications.

The comparison of continuum-removed radiance with ASTER spectra as a reference through NCC provided an estimate of the similarity level. The results indicated that continuum-removed radiance was highly consistent with the reference spectra. The NNLS algorithm showed higher similarity compared with the GD algorithm. This result indicates the difference between a constrained least-squares algorithm (in NNLS) and local minimum calculation in the GD algorithm, which resulted in a better response of NNLS to amplitude variations compared with the GD algorithm. However, the computational complexity of the GD calculation was lower than that of NNLS.

6. CONCLUSIONS

The approach proposed is a modification of the continuum removal process of spectral radiance for ground-based spectroscopy. It alleviates the calcu-

lation of the blackbody temperature on the panel's surface by conducting the acquisition before and after heating the samples. The calculation was verified by using data generated from an experiment conducted within the $7.7\mu\text{m}$ to $11.8\mu\text{m}$ LWIR wavelength range using a FIRST FTIR LW hyperspectral camera of Telops. Subsequent calculations of continuum removal were also modified by an estimation of the downwelling spectral radiance using NMF optimized by GD and NNLS. The result was then compared with the results obtained using spectral averaging and random selection of spectra in the presence of 1%~20% additive noise. The similarity percentage of the continuum-removed spectra with each method was compared with the spectra of the minerals from the ASTER spectral library by using SAM and NCC. The method was also subjected to 2%~15% wrong pixel spectrum selection of Infragold, and its similarity percentage was measured by SAM and NCC. The results showed a higher similarity value when NMF is used compared with the situation when the other approaches are utilized. In general, NMF-NNLS showed more robustness to noise in comparison with NMF-GD, averaging and random selection. The computation complexity of the proposed algorithms may be affected by other possible artifacts (e.g. inaccurate selection of reference radiance spectra). A cross-validation method to determine the number of iterations involved when applying NNLS and GD can be a subject for future work. Moreover, NMF can be employed with semi-optimized NMF using GD, NNLS or non-negative quadratic programming rules, which may improve the NMF calculation and its possible sensitivity to spectral radiance calculation.

ACKNOWLEDGMENT

The authors would thank anonymous reviewers and editor of Applied Optics journal for their constructive comments. Also we would like to acknowledge and thank Annette Schwerdtfeger from the Department of Electrical and Computer Engineering at Laval University for her constructive comments and help. This research was supported by FRQ-NT (Fonds de Recherche du Québec - Nature et Technologies) grant number: 2014-MI-182452 and conducted under the Canadian research chair in Multipolar Infrared Vision (MIVIM) and the Chaire de recherche industrielle CRSNG- Agnico-Eagle en exploration minérale.

REFERENCES

1. B. YOUSEFI, S. SOJASI, C. I. CASTANEDO, X. P. MALDAGUE, G. BEAUDOIN, and M. CHAMBERLAND, "Continuum removal for ground based Iwir hyperspectral infrared imagery applying non-negative matrix factorization," (2018).
2. N. M. Nasrabadi, "Hyperspectral target detection: An overview of current and future challenges," *IEEE Signal Processing Magazine* **31**, 34–44 (2014).
3. R. Mayer, F. Bucholtz, and D. Scribner, "Object detection by using "whitening/dewhiting" to transform target signatures in multitemporal hyperspectral and multispectral imagery," *IEEE transactions on geoscience and remote sensing* **41**, 1136–1142 (2003).
4. Y. Wang, F. Xie, and J. Wang, "Short-wave infrared signature and detection of aircraft in flight based on space-borne hyperspectral imagery," *Chinese Optics Letters* **14**, 122801 (2016).
5. M. T. Eismann and R. C. Hardie, "Stochastic spectral unmixing with enhanced endmember class separation," *Applied optics* **43**, 6596–6608 (2004).
6. F. Kruse, "Identification and mapping of minerals in drill core using hyperspectral image analysis of infrared reflectance spectra," *International journal of remote sensing* **17**, 1623–1632 (1996).
7. T. Yajima, K. Ohkawa, and S. Huzikawa, "Hyperspectral alteration mineral mapping using the posam method," in "Geoscience and Remote Sensing Symposium, 2004. IGARSS'04. Proceedings. 2004 IEEE International," , vol. 2 (IEEE, 2004), vol. 2, pp. 1491–1493.
8. C. O. Davis, "Airborne hyperspectral remote sensing," Tech. rep., NAVAL RESEARCH LAB WASHINGTON DC (2001).
9. E. Hirsch and E. Agassi, "Detection of gaseous plumes in ir hyperspectral images—performance analysis," *IEEE Sensors Journal* **10**, 732–736 (2010).
10. S. M. Thulin, M. J. Hill, and A. A. Held, "Spectral sensitivity to carbon and nitrogen content in diverse temperate pastures of australia," in "Geoscience and Remote Sensing Symposium, 2004. IGARSS'04. Proceedings. 2004 IEEE International," , vol. 2 (IEEE, 2004), vol. 2, pp. 1459–1462.
11. I. D. Sanches, C. R. Souza Filho, and R. F. Kokaly, "Spectroscopic remote sensing of plant stress at leaf and canopy levels using the chlorophyll 680nm absorption feature with continuum removal," *ISPRS Journal of Photogrammetry and Remote Sensing* **97**, 111–122 (2014).
12. A. M. Filippi and J. R. Jensen, "Effect of continuum removal on hyperspectral coastal vegetation classification using a fuzzy learning vector quantizer," *IEEE transactions on geoscience and remote sensing* **45**, 1857–1869 (2007).
13. L. Balick, A. Gillespie, A. French, I. Danilina, J.-P. Allard, and A. Mushkin, "Longwave thermal infrared spectral variability in individual rocks," *IEEE Geoscience and Remote Sensing Letters* **6**, 52–56 (2009).
14. L. Sun and S. Khan, "Ground-based hyperspectral remote sensing of hydrocarbon-induced rock alterations at cement, oklahoma," *Marine and Petroleum Geology* **77**, 1243–1253 (2016).
15. D. Krupnik, S. Khan, U. Okyay, P. Hartzell, and H.-W. Zhou, "Study of upper albian rudist buildups in the edwards formation using ground-based hyperspectral imaging and terrestrial laser scanning," *Sedimentary Geology* **345**, 154–167 (2016).
16. D. Akseanova, B. Yousefi, F. Larachi, X. P. Maldague, and G. Beaudoin, "Monitoring thermal phenomena in co2 capture by brucite," .
17. M. Ghasemzadeh-Barvarz, A. Ramezani-Kakroodi, D. Rodrigue, and C. Duchesne, "Multivariate image regression for quality control of natural fiber composites," *Industrial & Engineering Chemistry Research* **52**, 12426–12436 (2013).
18. P. B. Garcia-Allende, O. M. Conde, J. Mirapeix, A. M. Cubillas, and J. M. López-Higuera, "Data processing method applying principal component analysis and spectral angle mapper for imaging spectroscopic sensors," *IEEE Sensors Journal* **8**, 1310–1316 (2008).
19. D. C. Heinz, C. E. Davidson, and A. Ben-David, "Temporal-spectral detection in long-wave ir hyperspectral imagery," *IEEE Sensors Journal* **10**, 509–517 (2010).
20. K. C. Bradley, K. C. Gross, and G. P. Perram, "Imaging fourier transform spectrometry of combustion events," *IEEE Sensors Journal* **10**, 779–785 (2010).
21. B. Yousefi, S. Sojasi, C. I. Castanedo, G. Beaudoin, F. Huot, X. P. Maldague, M. Chamberland, and E. Lalonde, "Emissivity retrieval from indoor hyperspectral imaging of mineral grains," in "Thermosense: Thermal Infrared Applications XXXVIII," , vol. 9861 (International Society for Optics and Photonics, 2016), vol. 9861, p. 98611C.
22. J. W. Salisbury and N. Vergo, *Infrared (2.1-25 um) spectra of minerals* (Johns Hopkins University Press, 1991).
23. J. W. Salisbury, A. Wald, and D. M. D'Aria, "Thermal-infrared remote sensing and kirchhoff's law: 1. laboratory measurements," *Journal of Geophysical Research: Solid Earth* **99**, 11897–11911 (1994).
24. A. R. Korb, P. Dybwad, W. Wadsworth, and J. W. Salisbury, "Portable fourier transform infrared spectroradiometer for field measurements of radiance and emissivity," *Applied Optics* **35**, 1679–1692 (1996).
25. S. J. Hook and A. B. Kahle, "The micro fourier transform interferometer (μ ftir)—a new field spectrometer for acquisition of infrared data of natural surfaces," *Remote Sensing of Environment* **56**, 172–181 (1996).
26. S. W. Ruff, P. R. Christensen, P. W. Barbera, and D. L. Anderson, "Quantitative thermal emission spectroscopy of minerals: A laboratory technique for measurement and calibration," *Journal of Geophysical Research: Solid Earth* **102**, 14899–14913 (1997).
27. J. A. Sobrino, C. Mattar, P. Pardo, J. C. Jiménez-Muñoz, S. J. Hook, A. Baldrige, and R. Ibañez, "Soil emissivity and reflectance spectra measurements," *Applied optics* **48**, 3664–3670 (2009).
28. C. Gomez, P. Lagacherie, and G. Coulouma, "Continuum removal versus pls-r method for clay and calcium carbonate content estimation from laboratory and airborne hyperspectral measurements," *Geoderma* **148**, 141–148 (2008).
29. Z. Malenovský, L. Homolová, R. Zurita-Milla, P. Lukeš, V. Kaplan, J. Hanuš, J.-P. Gastellu-Etchegorry, and M. E. Schaepman, "Retrieval of spruce leaf chlorophyll content from airborne image data using continuum removal and radiative transfer," *Remote Sensing of Environment* **131**, 85–102 (2013).
30. O. Mutanga, A. K. Skidmore, and H. Prins, "Predicting in situ pasture quality in the kruger national park, south africa, using continuum-removed absorption features," *Remote sensing of Environment* **89**, 393–408 (2004).
31. Z. Huang, B. J. Turner, S. J. Dury, I. R. Wallis, and W. J. Foley, "Estimating foliage nitrogen concentration from himap data using continuum removal analysis," *Remote Sensing of Environment* **93**, 18–29 (2004).
32. "http://telops.com/products/hyperspectral-cameras/item/download/76_856bf981c221d53f5c8f73bffe75d6cb," (2016).
33. X. Maldague, "Theory and practice of infrared technology for nondestructive testing," (2001).
34. H. Zhang, L. Yu, U. Hassler, H. Fernandes, M. Genest, F. Robitaille, S. Joncas, W. Holub, Y. Sheng, and X. Maldague, "An experimental and analytical study of micro-laser line thermography on micro-sized flaws in stitched carbon fiber reinforced polymer composites," *Composites Science and Technology* **126**, 17–26 (2016).
35. "Labsphere: Technical guide: Integrating sphere theory and applications," <https://www.labsphere.com/site/assets/files/2553/a-guide-to-reflectance-materials-and-coatings.pdf>. Accessed 08 September 2017.
36. A. Resnick, C. Persons, and G. Lindquist, "Polarized emissivity and kirchhoff's law," *Applied optics* **38**, 1384–1387 (1999).
37. G. Kirchhoff, "I. on the relation between the radiating and absorbing powers of different bodies for light and heat," *The London, Edinburgh, and Dublin Philosophical Magazine and Journal of Science* **20**, 1–21 (1860).
38. G. H. Golub and C. F. Van Loan, *Matrix computations*, vol. 3 (JHU Press, 2012).
39. J. N. Franklin, *Matrix theory* (Courier Corporation, 2012).
40. K. Pearson, "Liii. on lines and planes of closest fit to systems of points in space," *The London, Edinburgh, and Dublin Philosophical Magazine and Journal of Science* **2**, 559–572 (1901).

41. I. T. Jolliffe, "Principal component analysis and factor analysis," in "Principal component analysis," (Springer, 1986), pp. 115–128.
42. Y. Panagakis, C. Kotropoulos, and G. R. Arce, "Non-negative multilinear principal component analysis of auditory temporal modulations for music genre classification," *IEEE Transactions on Audio, Speech, and Language Processing* **18**, 576–588 (2010).
43. S. Sra and I. S. Dhillon, "Generalized nonnegative matrix approximations with bregman divergences," in "Advances in neural information processing systems," (2006), pp. 283–290.
44. C. Ding, "Spectral clustering, principal component analysis and matrix factorizations for learning," in "Int'l Conf. on Machine Learning (Tutorial)," (2005).
45. D. D. Lee and H. S. Seung, "Learning the parts of objects by non-negative matrix factorization," *Nature* **401**, 788–791 (1999).
46. C. Ding, X. He, and H. D. Simon, "On the equivalence of nonnegative matrix factorization and spectral clustering," in "Proceedings of the 2005 SIAM International Conference on Data Mining," (SIAM, 2005), pp. 606–610.
47. B. Yousefi, S. Sojasi, C. I. Castanedo, X. P. Maldague, G. Beaudoin, and M. Chamberland, "Comparison assessment of low rank sparse-pca based-clustering/classification for automatic mineral identification in long wave infrared hyperspectral imagery," *Infrared Physics & Technology* (2018).
48. K. C. Kiwiel, "Convergence and efficiency of subgradient methods for quasiconvex minimization," *Mathematical programming* **90**, 1–25 (2001).
49. Y.-C. Cho and S. Choi, "Nonnegative features of spectro-temporal sounds for classification," *Pattern Recognition Letters* **26**, 1327–1336 (2005).
50. D. Chen and R. J. Plemmons, "Nonnegativity constraints in numerical analysis," in "The birth of numerical analysis," (World Scientific, 2010), pp. 109–139.
51. H. Kim and H. Park, "Nonnegative matrix factorization based on alternating nonnegativity constrained least squares and active set method," *SIAM journal on matrix analysis and applications* **30**, 713–730 (2008).
52. F. A. Kruse, A. Lefkoff, J. Boardman, K. Heidebrecht, A. Shapiro, P. Barloon, and A. Goetz, "The spectral image processing system (sips)—interactive visualization and analysis of imaging spectrometer data," *Remote sensing of environment* **44**, 145–163 (1993).
53. A. Baldridge, S. Hook, C. Grove, and G. Rivera, "The aster spectral library version 2.0," *Remote Sensing of Environment* **113**, 711–715 (2009).
54. V. Franc, V. Hlaváč, and M. Navara, "Sequential coordinate-wise algorithm for the non-negative least squares problem," in "CAIP," , vol. 3691 (Springer, 2005), pp. 407–414.
55. B. Yousefi, "Continuum removal," http://vision.gel.ulaval.ca/~bardia/PublicCodes/web_J0_29May2018.zip (2018).